Journal of Geophysical Research: Space Physics

RESEARCH ARTICLE
10.1029/2018JA025559

The Improved Two-Dimensional Artificial Neural Network-Based Ionospheric Model (ANNIM)

S. Tulasi Ram[1], V. Sai Gowtam[1], Arka Mitra[2], and B. Reinisch[3,4]

[1]Indian Institute of Geomagnetism, Navi Mumbai, India, [2]Department of Atmospheric Sciences, University of Illinois, Urbana, IL, USA, [3]Lowell Digisonde International, Lowell, MA, USA, [4]Center for Atmospheric Research, University of Massachusetts, Lowell, MA, USA

Key Points:
- Improved artificial neural network-based 2-D ionospheric model (ANNIM) using climatological GPS-RO and Digisonde data is presented
- The improved ANNIM better represents the spatial and temporal variations of NmF2 and hmF2 including prereversal enhancement (PRE)
- Improved ANNIM successfully predicts the NmF2/hmF2 response to recurrent geomagnetic activity and distinguishes the roles of Kp and F10.7

Correspondence to:
S. Tulasi Ram,
tulasi@iigs.iigm.res.in

Citation:
Tulasi Ram, S., Sai Gowtam, V., Mitra, A., & Reinisch, B. (2018). The improved two-dimensional artificial neural network-based ionospheric model (ANNIM). *Journal of Geophysical Research: Space Physics*, *123*, 5807–5820. https://doi.org/10.1029/2018JA025559

Received 9 APR 2018
Accepted 13 JUN 2018
Accepted article online 27 JUN 2018
Published online 14 JUL 2018

Abstract An artificial neural network-based two-dimensional ionospheric model (ANNIM) that can predict the ionospheric F2-layer peak density (NmF2) and altitude (hmF2) had recently been developed using long-term data of Formosat-3/COSMIC GPS radio occultation (RO) observations (Sai Gowtam & Tulasi Ram, 2017a, https://doi.org/10.1002/2017JA024795). In this current paper, we present an improved version of ANNIM that was developed by assimilating additional ionospheric data from CHAMP, GRACE RO, worldwide ground-based Digisonde observations, and by using a modified spatial gridding approach based on the magnetic dip latitudes. The improved ANNIM better reproduces the spatial and temporal variations of NmF2 and hmF2, including the postsunset enhancement in equatorial hmF2 associated with the prereversal enhancement in the zonal electric field. The ANNIM-predicted NmF2 and hmF2 exhibit excellent correlations with ground-based Digisonde observations over different solar activity periods. The ANNIM simulations under enhanced geomagnetic activity predict the depletion of NmF2 at auroral-high latitudes, and enhancement over low latitude to midlatitude with respect to quiet conditions, which is consistent with the storm time meridional wind circulation and the associated neutral composition changes. The improved ANNIM also predicts a significant enhancement in hmF2 around auroral latitudes due to increased plasma scale height associated with particle and Joule heating during storm periods. Further, the ANNIM successfully reproduces the coherent oscillations in NmF2 and hmF2 with recurrent cororating interaction region-driven geomagnetic activity during the extreme solar minimum year 2008 and can distinguish the roles of recurrent geomagnetic activity and solar irradiance through controlled simulations.

1. Introduction

The plasma density in the terrestrial ionosphere exhibits complex spatial (latitude, longitude, and altitude) and temporal (local time, season, and solar cycle epoch) variability even under quiet geomagnetic conditions. Because the neutral-dynamic and electro-dynamic transport processes become dominant relative to the photochemical reactions, the *F* region of the ionosphere exhibits large scale anomalies like the equatorial ionization anomaly (EIA; Appleton, 1946), ionospheric annual anomaly (Berkner & Wells, 1938; Sai Gowtam & Tulasi Ram, 2017b), the winter anomaly (Burns et al., 2014; Rishbeth & Setty, 1961; Sai Gowtam & Tulasi Ram, 2017c), and the midlatitude summer nighttime anomaly (Bellchambers & Piggott, 1958; Lin et al., 2010; Liu et al., 2010). Lower atmospheric wave forces such as gravity waves, planetary waves, and atmospheric tides can also cause notable modifications in the ionospheric plasma distribution (e.g., Brahmanandam et al., 2011; Lin et al., 2007; Wan et al., 2008). Added to this quiet time variability, the ionospheric electron density also undergoes dramatic changes during active space weather events such as coronal mass ejections, high-speed solar wind streams (HSS), and the associated geomagnetic storms. Through extensive research, the scientific community has been steadily building the crucial scientific understanding of quiet and disturbed time variability of the ionosphere and its effects on technological systems such as long-distance high-frequency communications, electrical power grids, payloads onboard satellites, and satellite-based augmentation systems (e.g., Balan et al., 2015, 2017; Baker et al., 2013; Gaunt & Coetzee, 2007; MacAlester & Murtagh, 2014; Tulasi Ram et al., 2015; Tulunay & Bradley, 2004). Significant progress has also been made in the modeling of the ionosphere using both physics-based first principles models as well as data-driven empirical models (Anderson et al., 1998; Bilitza et al., 2017; Bust & Mitchell, 2008; Schunk, 2013 and reference therein). Physics-based models solve the continuity, momentum, and energy equations of ionospheric species and predict the spatial and temporal variability of the ionosphere under varying background conditions such as electric fields, neutral winds, solar activity, and geomagnetic

activity. TIEGCM (Thermosphere Ionosphere Electrodynamics General Circulation Model), CTIM (Coupled Thermospheric Ionospheric Model), SUPIM (Sheffield University Plasmaspheric Ionospheric Model), and SAMI2/SAMI3 (SAMI2/SAMI3 is Another Model of the Ionosphere) are some of the prominent physics-based models (Bailey & Balan, 1996; Fuller-Rowell et al., 1996; Huba et al., 2000, 2008; Richmond et al., 1992). Data-driven empirical models, on the other hand, assimilate large databases and predict the model parameters by fitting the data with a set of controlling input parameters using predefined analytical functions, for example, IRI (International Reference Ionosphere) and NeQuick (Bilitza et al., 2017; Radicella & Leitinger, 2001). However, because of several linear and nonlinear processes that are simultaneously contributing at different magnitudes and polarity, accurate modeling and/or forecasting of the ionosphere under varying space weather conditions is still a challenging task ahead of the scientific community (Anderson et al., 1998 and Schunk 2013).

With the recent advancements in artificial intelligence, another approach that could be effective in data driven empirical models is the systematic machine learning technique with artificial neural networks (ANNs). In this approach, the neural networks are systematically trained using climatological ionospheric databases with a set of controlling input parameters. Quite a few studies have successfully implemented the ANNs to predict the ionospheric parameters such as peak electron density (NmF2) and critical frequency (foF2; Altinay et al., 1997; Kumluca et al., 1999; Lamming & Cander, 1999; Oyeyemi & Poole, 2004; Oyeyemi et al., 2005; Williscroft & Poole, 1996; Wintoft, 2000; Zhao et al., 2014; Zhou et al., 2013) and total electron content (Habarulema et al., 2011; Leandro & Santos, 2007; Ma et al., 2005; Tulunay et al., 2006; Watthanasangmechai et al., 2012) indicating the potential application of ANNs for modeling the ionosphere. Recently, a more comprehensive global two-dimensional ionospheric model to predict NmF2 and hmF2 called ANNIM (ANN-based Ionospheric Model) has been developed by Sai Gowtam and Tulasi Ram (2017a) (further referred, in short, as ST2017) using the long-term and global GPS-RO (Global Positioning System-radio occultation) data set from the Formosat-3/COSMIC (F3/C) mission. ST2017 have implemented the feed-forward neural network with error back propagation algorithm (Levenberg, 1944; Marquardt, 1963; Rumelhart et al., 1986) with one hidden layer of 40 neurons (readers may please refer to ST2017 for more details). Further, ST2017 have implemented the "gridded neural networks" approach where the global ionospheric data are divided into 324 smaller spatial grids of size 20° longitude × 10° latitude in geographic coordinates. Each spatial grid is individually trained using the neural networks, and the set of 324 trained networks are then combined using a front-end MATLAB code to construct the 2-D model. The ANNIM was found to successfully predicting the local time, latitude, longitude, and seasonal variations of NmF2/hmF2, and also capturing the large-scale ionospheric anomalies like EIA, ionospheric annual anomaly, Weddell Sea anomaly, and midlatitude summer nighttime anomaly. However, the ANNIM has failed to reproduce the postsunset enhancement in hmF2 at equatorial latitudes (Figures 7d and 7e of ST2017). Further, ST2017 have only presented the ANNIM predictions under quiet geomagnetic conditions and have not evaluated the performance of ANNIM under varying solar and geomagnetic activity conditions.

In this paper, we present the improved version of the two-dimensional ANNIM constructed with the inclusion of additional ionospheric data and using the modified spatial grids based on the dip latitudes. The data and methodology used in the improved ANNIM are presented in section 2. The learning capability of ANN architecture and the performance of the improved ANNIM are evaluated in comparison with ground-based Digisonde measurements and the IRI-2016 model (http://irimodel.org/IRI-2016/) under varying solar activity conditions in section 3.1. The local time, latitude, and seasonal variations of NmF2 and hmF2 predicted by the improved ANNIM are presented in section 3.2. Further, the ANNIM response under quiet and disturbed geomagnetic conditions are compared and qualitatively discussed in section 3.3. Also, the global NmF2 and hmF2 variations predicted by the ANNIM in response to recurrent geomagnetic activity during the deep solar minimum year 2008 have been evaluated through controlled simulations of ANNIM and Lomb-Scargle spectral analysis in section 3.4. Finally, the important features of the improved ANNIM are summarized, and conclusions are drawn in section 4.

2. Data and Methodology

ST2017 have used the globally distributed vertical electron density profile Ne (h) data from the F3/C RO mission for 2006–2015. In addition to the F3/C data, the GPS-RO observations from CHAMP (available during 2002 to 2008) and GRACE (2007 to 2015) have also been considered in this study. The RO electron density

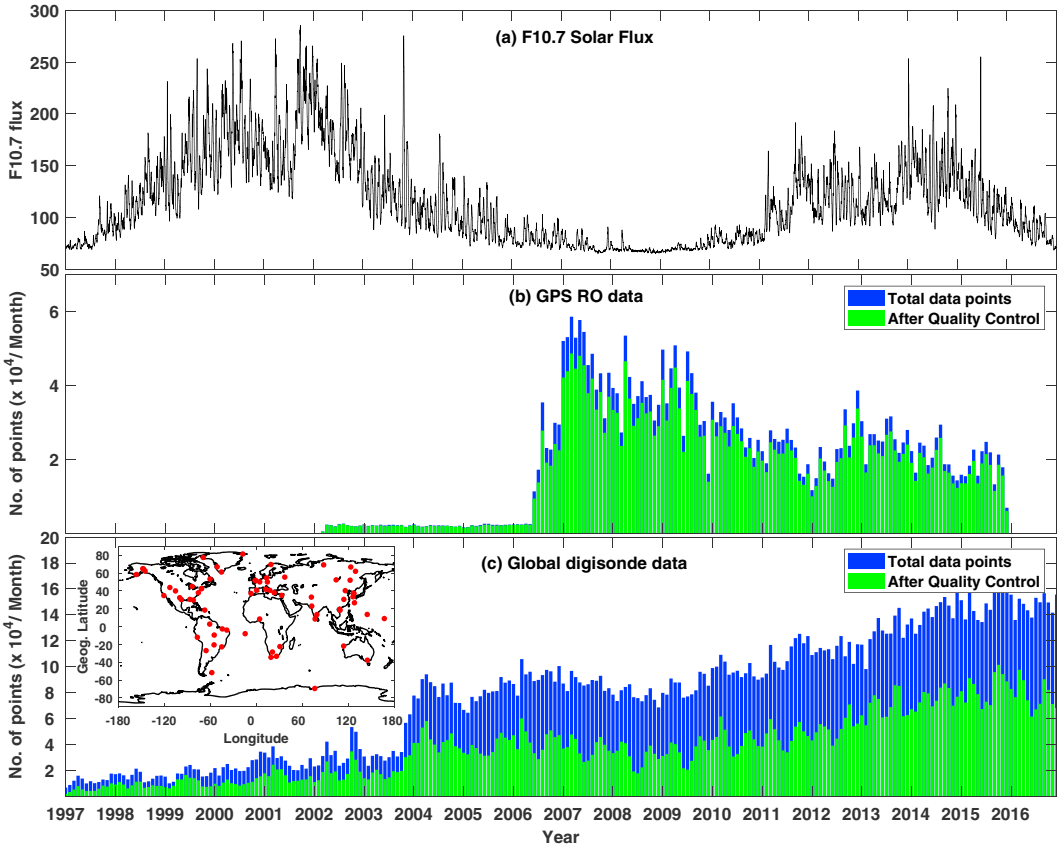

Figure 1. (a) Daily averaged F10.7 solar flux values during the study; (b) data statistics of GPS-radio occultation data obtained from the CHAMP, GRACE and FORMOSAT-3/COSMIC; and (c) data statistics of the global Digisonde observations. The inset in Figure 1(c) shows the geographical distribution of Digisondes in the GIRO network. The blue color bars indicate total number of observations and the green color bars indicate the data points after quality control measures.

profiles are found to be in good agreement with ground-based incoherent scatter radar and ionosonde observations (Lei et al., 2007; Schreiner et al., 2007). All the RO profiles initially underwent quality control checks, and the bad profiles with a mean standard deviation higher than 1.5 and/or the F2-layer peak height below 200 km or above 500 km have been excluded from the analysis as suggested in Yang et al. (2009), Potula et al. (2011), and Uma et al. (2016). The F3/C together with CHAMP and GRACE observations (http://cdaac-www.cosmic.ucar.edu) provides ~1,500–2,000 observations per day that are more or less uniformly distributed over the globe during the years 2006 to 2015. In addition to the GPS-RO data, the scaled NmF2 and hmF2 data from the Digisonde Global Ionosphere Radio Observatory (GIRO; Reinisch et al., 2009; Reinisch & Galkin, 2011) for the period from 1997 to 2016 have also been considered (http://giro.uml.edu/didbase/scaled.php). The GIRO NmF2 and hmF2 data were automatically derived from the autoscaled ionogram echo traces using ARTIST-5 software (Galkin et al., 2008). In the present analysis, only autoscaled data points with a confidence score of 90 and above are considered in order to avoid the scaling errors during spread-*F* periods and other noisy ionogram traces. Figure 1 illustrates the quantum of data used in the present study. Figure 1a shows the daily variation of F10.7 solar flux from 1997 to 2016. Figure 1b shows the number of GPS-RO observations per month from the F3/C, CHAMP, and GRACE together. The blue bars indicate the total number of available data points, and the green bars indicate the number of data points after the quality control measures mentioned above. It can be observed that the number of GPS-RO observations increased drastically from the middle of 2006 with the introduction of the F3/C satellite constellation. The number of GPS-RO observations during 2011 and later years are gradually decreasing due to the operational failure of some of the F3/C satellites (http://cdaac-www.cosmic.ucar.edu/cdaac/index.html). Figure 1c shows the number of data points in each month from the GIRO Digisonde network from 1997 to 2016. The geographical distribution of the Digisondes under GIRO

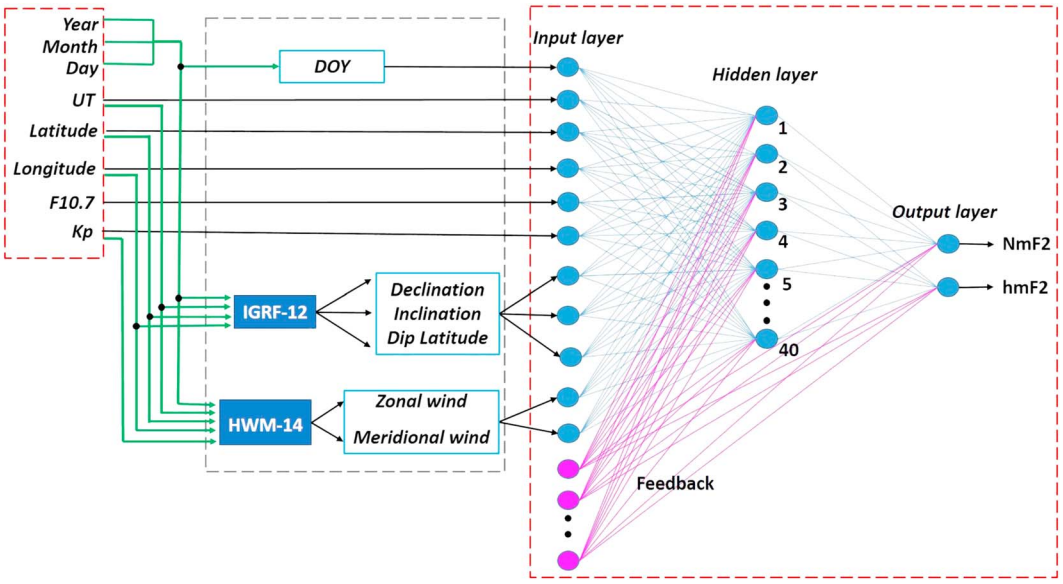

Figure 2. Architecture of feed-forward neural network used in the ANNIM model (Sai Gowtam & Tulasi Ram, 2017a).

network is shown in the inset of Figure 1c. The blue bars indicate the total number of autoscaled data points available from GIRO-DIDBase, and the green bars indicate the data points after the quality control check for the confidence score greater than 90 as mentioned above. It can be noticed from Figure 1c that the Digisonde data are steadily increasing from 1997 to 2016 with the additions of more Digisondes in the network. The combined GPS-RO and GIRO-DIDBase data form a large database of NmF2 and hmF2 values that spans a wide range of solar activity, with a significantly larger quantity of data covering the declining phase of solar cycle 23 and solar cycle 24 (2004 to 2016). The daily mean values of F10.7 solar flux and Kp index (3-hourly) data have been obtained from National Aeronautics and Space Administration (NASA)'s space physics data facility (https://omniweb.gsfc.nasa.gov).

In the present work, the globally distributed NmF2 and hmF2 data from the GPS-RO missions and the Digisonde network are divided into a total of 840 smaller spatial grids of size 5° dip latitude and 15° geographic longitudes. The data in each spatial grid are trained separately using neural network of the same architecture that was used in ST2017. For the benefit of the readers, we are presenting the neural network architecture once again in Figure 2 and briefly explain it here. The controlling input parameters of the neural network consist of date (YYYY/MM/DD) or day of the year (DOY), universal time (UT), geographic latitude, geographic longitude, F10.7 solar flux, and Kp index. These inputs are also fed to IGRF-2012 (International Geomagnetic Reference Field; Thébault et al., 2015) model to compute geomagnetic declination, inclination, and dip latitudes, and also fed to HWM-2014 (Horizontal Wind Model) (Drob et al., 2015) to estimate the zonal and meridional neutral winds through an internal subroutine (grey box, Figure 2). Therefore, the final inputs to the input layer of neural network are DOY, UT, latitude, longitude, F10.7, Kp, declination, inclination, dip latitude, zonal wind, and meridional wind. The targets of the neural networks (output layer) are F2-layer peak density (NmF2) and altitude (hmF2).

The implementation of ANN involves a multivariate regression of the targets (NmF2 and hmF2 data) with the above given set of controlling input parameters by initially assigning different weights to input parameters and neurons in the hidden layer. Then the machine learning process systematically changes the weights of inputs and neurons iteratively until the best regression is achieved between the targets and input parameters. During this learning process, the total data are randomly divided into three data sets, called training, validation, and testing data sets with 70%, 15%, and 15% of data, respectively. The training set is used to derive a nonlinear relationship between the inputs and targets, and estimates the weights. The validation set is used to validate the network performance by estimating the errors. This validation process avoids the overfitting of model parameters and ensures that the errors are within the permissible range. The testing data set, which is independent from training and validation, is used to evaluate the overall learning efficiency

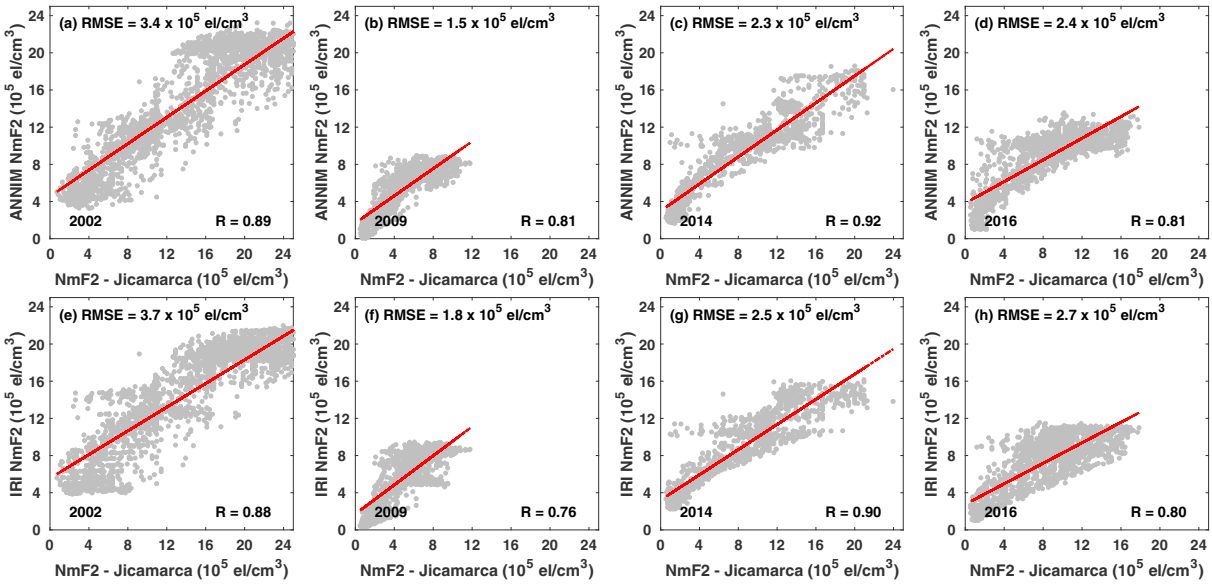

Figure 3. The comparisons of (top panels) ANNIM and (bottom panels) IRI-2016 predicted NmF2 values with the ground-based Digisonde observations over Jicamarca. The red straight lines indicate the linear regression between the ANNIM/IRI predictions and Digisonde data.

by analyzing the regression between the actual targets and predicted outputs, and sends the feedback to the network. This training-validation-testing cycle, collectively known as "learning," is repeated iteratively until the optimum regression is achieved. After several test runs by varying the number of neurons in the hidden layer and analyzing the regression and RMS (root-mean-square) errors between the targets and model outputs, we found that the neural network consisting of one hidden layer with 40 neurons gives the optimum regression and least RMS error. In this study, we have adopted the feed-forward neural network with error back propagation algorithm because of its ability to solve more complex problems and faster learning speeds (Krasnopolsky & Lin, 2012; Rumelhart et al., 1986) as shown in Figure 2 (red box). Finally, a total of 840 trained networks (one for each spatial grid) are combined through a front-end subroutine to construct the improved ANNIM.

3. Results and Discussion

3.1. Comparison With Digisonde Data and IRI-2016 Model Under Different Solar Activity Conditions

ST2017 have evaluated the learning efficiency of the above neural network architecture by thoroughly comparing the ANNIM-predicted NmF2 and hmF2 values with the original F3/C data and also with the independent data of GRACE RO observations. They have also validated the ANNIM predictions of local time, latitude, and longitudinal variations of NmF2 and hmF2 and found that they are in good agreement with the respective variations derived from the F3/C data. In the present paper, we further evaluate the performance of the improved ANNIM in comparison with the ground-based Digisonde observations as well as the IRI-2016 model (International Reference Ionosphere, http://irimodel.org/) (Bilitza et al., 2017). For this purpose, the NmF2 and hmF2 data during a 40-day window centered over March equinox (DOY between 60 and 100) in different solar activity years 2002, 2009, 2014, and 2016 are obtained from a Digisonde at an equatorial station, Jicamarca. The years 2002 and 2014 correspond to solar maximum years of solar cycles 23 and 24, respectively, and the years 2009 and 2016 correspond to very low activity years. The average F10.7 solar flux for the selected 40-day window periods in 2002, 2009, 2014, and 2016 are 188, 69, 147, and 82 solar flux units, respectively. It should be noted that the selected Digisonde NmF2 and hmF2 data correspond to the different UT times, DOY (between 60 and 100), F10.7 solar flux, and Kp-index values. The ANNIM and the IRI-2016 models have run for the same UT times, DOY, F10.7, and Kp values of the actual data, and the ANNIM and IRI-2016 predictions are compared with the measured Digisonde data in Figures 3 and 4.

The top panels of Figure 3 show the ANNIM-predicted NmF2 values in comparison with the ground-based Digisonde observations for the years 2002, 2009, 2014, and 2016 (Figures 3a–3d, respectively). The red

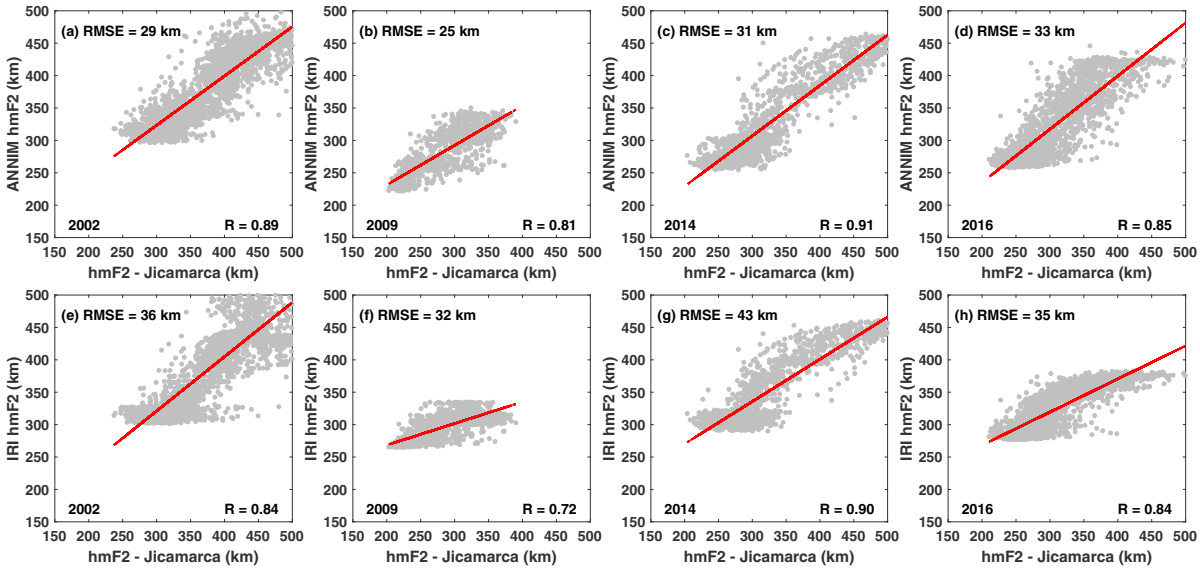

Figure 4. Similar as Figure 3 but for hmF2.

straight lines indicate the linear regression between the ANNIM predictions and Digisonde data. The regression coefficients (*R*) and the RMS errors (RMSE) of ANNIM predictions with respect to Digisonde data are indicated in Figures 3a–3d. It can be observed from these figures that the ANNIM predictions exhibit good linear correlations with the Digisonde data during all the years with regression coefficients (*R*) varying from 0.81 to 0.92. The RMSE in the ANNIM predictions vary from 1.5×10^5 electrons/cm^3 during deep solar minimum year 2009 to 3.4×10^5 electrons/cm^3 during the high solar activity year 2002. Figures 3e and 3h (bottom panels) show similar comparisons between the IRI-2016-predicted NmF2 and Digisonde observations for the years 2002, 2009, 2014, and 2016. The regression coefficients for IRI-2016 model predictions varies between 0.76 to 0.9, and the RMSE values are found to vary from 1.8×10^5 electrons/cm^3 during 2009 to 3.7×10^5 electrons/cm^3 during 2002. From the comparisons of ANNIM and IRI-2016 model predictions with respect to ground-based Digisonde observations, it can be noticed that the predictions of ANNIM are as good as IRI-2016 model. Similarly, Figure 4 shows the comparisons of ANNIM- (top panels) and IRI-2016 (bottom panels)-predicted hmF2 values with the ground-based Digisonde observations at Jicamarca. It can be observed from these figures that both ANNIM- and IRI-2016-predicted hmF2 values exhibit good linear correlations with the ground-based Digisonde data during all the years. Further, the regression coefficients are slightly higher (and RMS errors are slightly smaller) in ANNIM predictions compared to IRI-2016 predictions. Therefore, from the validations with the ground-based Digisonde observations shown in Figures 3 and 4, and also with the GPS-RO observations presented in ST2017, it can be concluded that the learning efficiency of the above neural network architecture is good, and the ANNIM predictions are as good as IRI-2016 which may be a slightly better performance by the ANNIM. In the remainder of this paper, we present the ANNIM responses under varying temporal, spatial, and geomagnetic activity conditions and describe the important features predicted by this model.

3.2. Local Time and Dip Latitude Variations of Zonally Averaged NmF2 and hmF2

The top panels of Figure 5 show the local time variations of zonally (longitudinally) averaged NmF2 predicted by ANNIM under quiet geomagnetic activity (Kp = 2) and moderate solar activity (F10.7 solar flux = 120 sfu) conditions. The left panels (Figures 5a and 5d) correspond to March equinox (DOY = 80), the middle panels (Figures 5b and 5e) correspond to June solstice (DOY = 172), and the right panels (Figures 5c and 5f) correspond to December solstices (DOY = 355). The solid black line represents the dip equator. From the Figures 5a and 5c, one can observe that the ANNIM has well reproduced the spatial and temporal variations of NmF2. For example, Figure 5a shows a well-developed and symmetrical EIA during the March equinox. During

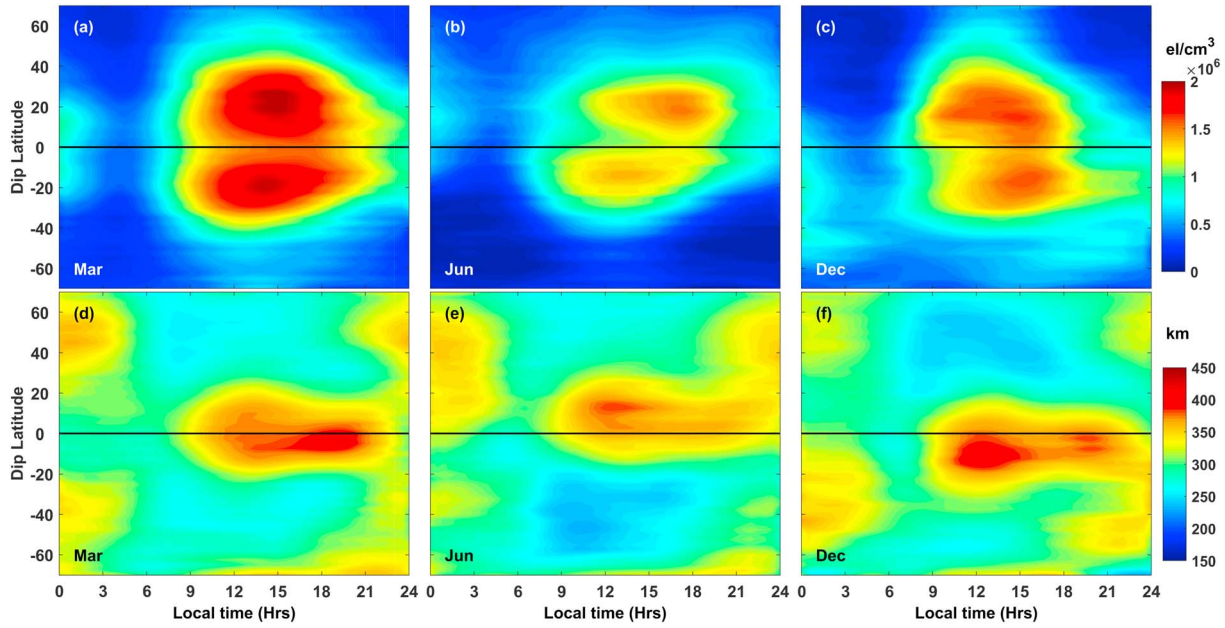

Figure 5. Local time and dip latitudinal variation of zonally averaged (top panels) NmF2 and (bottom panels) hmF2 predicted by ANNIM during (left panels) March equinox, (middle panels) June solstice, and (right panels) December solstice at constant solar flux (F10.7 = 120 sfu).

June solstice (Figure 5b), one can clearly observe that the asymmetric EIA with NmF2 values in the southern (winter) EIA latitudes are higher than in the northern (summer) EIA latitudes during morning to noon hours (06–12 LT). Whereas in the afternoon hours, the NmF2 values in the northern (summer) EIA latitudes becomes higher than in the southern (winter) EIA latitudes. Similar hemispheric asymmetries in the EIA with higher NmF2 values in the winter (northern) hemispheric low latitudes during the morning hours and in the summer (southern) hemispheric low latitudes during the afternoon hours can also be seen during December solstice as well (Figure 5c). This diurnal variation in the hemispheric asymmetry of EIA during solstices is mainly due to the interaction between summer-to-winter hemispheric neutral wind and the equatorial fountain process (Lin et al., 2007; Tulasi Ram et al., 2009) and is well reproduced by the ANNIM. Further, the overall NmF2 values during December solstice (Figure 5c) are significantly higher than June solstice (Figure 5b), which is known as the ionospheric annual anomaly (Berkner & Wells, 1938; Sai Gowtam & Tulasi Ram, 2017b). Therefore, from Figures 5a and 5c, one can conclude that the ANNIM has successfully reproduced the large-scale ionospheric features such as EIA and its hemispheric asymmetries during solstices and ionospheric annual anomaly.

The bottom panels of Figure 5 show the similar variations of zonally averaged hmF2. It can be seen from these figures that the hmF2 over equatorial and low-latitude regions exhibits an increase from morning to postsunset hours (9 to 21 LT). This increase in hmF2 over equatorial and low latitudes can be attributed to upward E × B drift due to a primary dawn-to-dusk zonal electric field during day time and the prereversal enhancement of zonal electric field (PRE) during postsunset hours. Further, it can be observed that the increase in hmF2 is symmetrical over the dip equator during the equinox (Figure 5d), whereas it is shifted to the low latitudes of the respective summer hemisphere during June and December solstices (Figures 5e and 5f). This increase in hmF2 at summer hemispheric low-latitudes during solstices is mainly due to the interaction between the field-aligned plasma transport by summer-to-winter hemispheric neutral wind and equatorial plasma fountain process as explained in Sai Gowtam and Tulasi Ram (2017b). Therefore, from Figures 5d and 5f, one can conclude that the ANNIM has successfully captured the local time, seasonal, and dip latitude variations for hmF2. The important improvement in this version of ANNIM (with respect to that of ST2017) is the enhanced hmF2 during postsunset hours due to PRE. This improvement is achieved by the smaller and dip latitude based spatial grids used in the gridded neural network approach incorporated in this version as described in section 2.

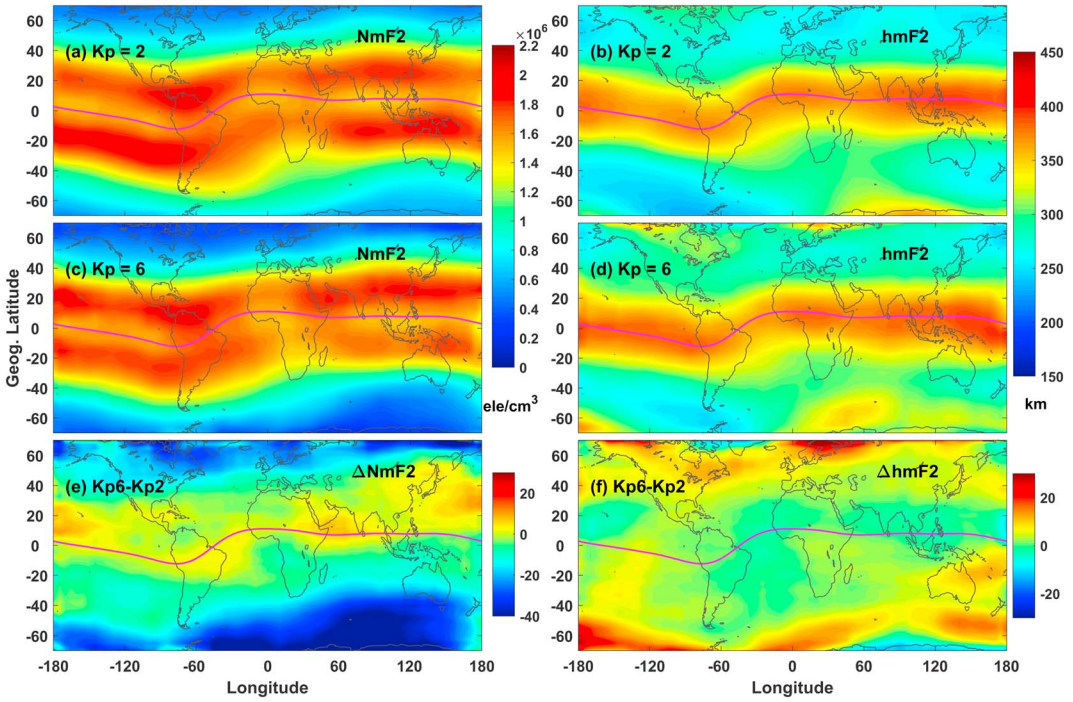

Figure 6. Longitudinal and geographic latitudinal variation of (left panels) NmF2 and (right panels) hmF2 predicted by ANNIM during (top panels) quiet (Kp-index = 2), (middle panels) disturbed (Kp-index = 6) geomagnetic conditions, and the (bottom panels) difference between disturbed and quiet time values in percentage with respect to background values.

3.3. ANNIM Predictions Under Quiet and Disturbed Geomagnetic Activity

With a view to further evaluate the ANNIM performance under quiet and disturbed geomagnetic conditions, we have performed controlled ANNIM model simulations for the March equinox (DOY = 80) conditions at two different Kp-index values (Kp = 2 and Kp = 6) by keeping a constant solar flux value (F10.7 = 120 sfu). The global ionospheric NmF2 and hmF2 maps corresponding to 12 LT are simulated using ANNIM. For example, the top panels show the longitudinal and latitudinal variations of NmF2 (Figure 6a) and hmF2 (Figure 6b) at a fixed local time of 12 LT during quiet (Kp = 2) geomagnetic conditions. The middle panels show similar spatial variations of NmF2 (Figure 6c) and hmF2 (Figure 6d) under disturbed (Kp = 6) geomagnetic conditions. The bottom panels (Figures 6c and 6f) show the changes in the NmF2 and hmF2 (ΔNmF2 and ΔhmF2) due to disturbed geomagnetic activity with respect to quiet time ionosphere and expressed in percentage as

$$\Delta \mathrm{NmF2} = \frac{\mathrm{NmF2_d} - \mathrm{NmF2_q}}{\mathrm{NmF2_q}} \times 100 \tag{1}$$

$$\Delta \mathrm{hmF2} = \frac{\mathrm{hmF2_d} - \mathrm{hmF2_q}}{\mathrm{hmF2_q}} \times 100 \tag{2}$$

where $\mathrm{NmF2_q}$ ($\mathrm{hmF2_q}$) and $\mathrm{NmF2_d}$ ($\mathrm{hmF2_q}$) represent the quiet (Kp = 2) and disturbed (Kp = 6) time NmF2 (hmF2). From Figure 6c, it can be seen that the NmF2 values around the equatorial and low latitude to midlatitude region are enhanced by about 5–15% during disturbed geomagnetic conditions. On the other hand, the NmF2 values around auroral latitude regions are significantly reduced by ~30–40% compared to the quiet time values. Similarly, from Figure 6f, the hmF2 values show large enhancement of the order of 25–30% around auroral latitudes in both southern and northern hemispheres. In the low latitude to midlatitude regions, the hmF2 variations exhibit only a slight enhancement with respect to the quiet time hmF2 values, as discussed in the following paragraph.

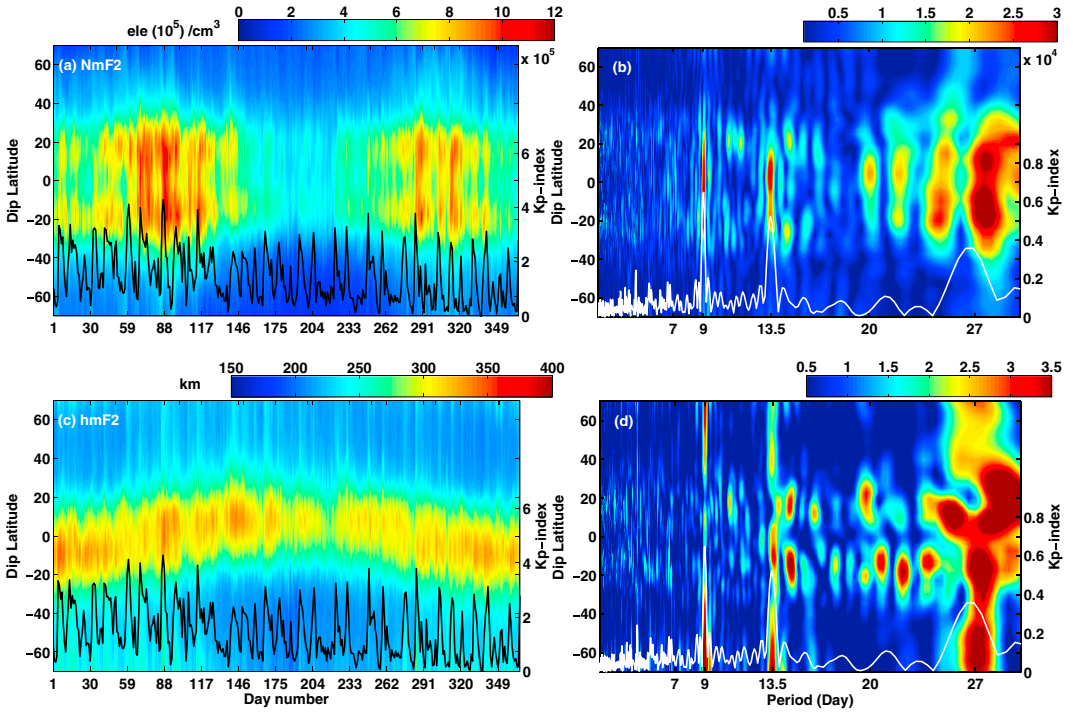

Figure 7. Dip latitude variation of zonally averaged day time (a) NmF2 and (b) hmf2 as a function of day number and the corresponding Lomb-Scargle periodogram of (c) NmF2 and (d) hmf2. The superimposed black curves in left panels indicate the daily averaged Kp-index. The white curves in right panels indicate the periodogram of daily averaged Kp-index.

The negative ionospheric storm effect (decrease in NmF2) at auroral latitudes can be attributed to the enhanced O/N2 ratio. The particle precipitation at auroral latitudes causes Joule heating and sets the meridional wind circulation (Fuller-Rowell et al., 1994). The upwelling neutral winds at high latitudes carry molecular rich air upwards causing a decrease in O/N2 ratio (Crowley et al., 2008; Fuller-Rowell et al., 1994) that increases the recombination loss of plasma at F2-peak altitudes as observed as largely depleted NmF2 values around auroral latitudes when Kp = 6 in Figure 6b (ΔNmF2 of -10 to -40% in Figure 6c). The downwelling neutral winds carry atomic oxygen (O) rich air to low latitudes and cause an increasing plasma density at F2-peak altitudes leading to a positive ionospheric storm at low latitude to midlatitude (Crowley et al., 2008; Strickland et al., 2001). This is consistent with the higher NmF2 values at low latitude to midlatitude in Figure 6b (ΔNmF2 of 5 to 15% in Figure 6c). The Joule heating due to enhanced particle precipitation also causes thermal expansion via increased neutral and plasma scale heights (Lei, Thayer, Forbes, Sutton, & Nerem, 2008; Lei, Thayer, Forbes, Sutton, Nerem, et al., 2008; Sojka et al., 2009; Thayer et al., 2008). The thermal expansion due to Joule and particle heating causes an enhancement in hmF2 at auroral and high latitudes (Tulasi Ram, Lei, et al., 2010 and Tulasi Ram, Liu, et al., 2010) is observed as a ~25 to 30% increase in hmF2 in Figure 6f. Therefore, the predicted variations in the NmF2 and hmF2 by the ANNIM with the enhanced geomagnetic activity are consistent with the earlier reports.

3.4. ANNIM Response for Recurrent Geomagnetic Activity

In this section we qualitatively evaluate the ANNIM response under recurrently varying geomagnetic activity conditions. Tulasi Ram, Lei, et al., (2010) and Tulasi Ram, Liu, et al., (2010) have studied the global ionospheric response to recurrent cororating interaction region (CIR)-driven geomagnetic activity during the deep solar minimum year 2008. They have shown that the ionospheric peak electron density (NmF2) and height (hmF2) are coherently ringing at solar rotational (27-day) and its subharmonic (13.5- and 9-day) periodicities due to recurrent HSS from the coronal holes and the associated recurrent CIR-driven geomagnetic activity. For example, Figures 7a and 7b show the dip latitude variations of zonally averaged day time NmF2 and hmF2, respectively, as a function of day number in 2008. These figures are constructed by zonally averaging the NmF2 and hmF2 from all the available data sources F3/C, CHAMP, GRACE RO observations, and ground-

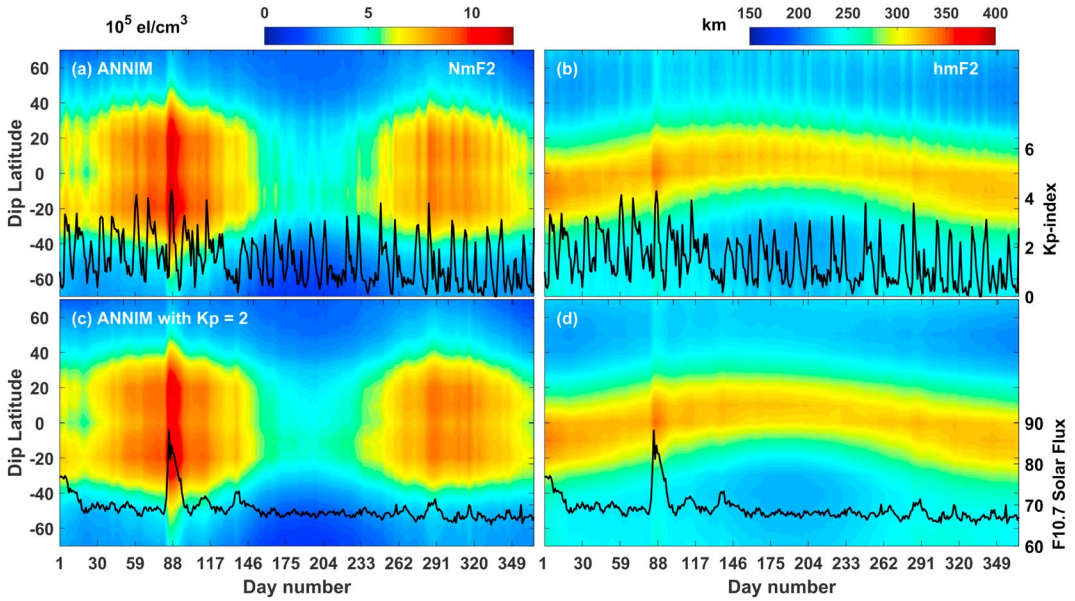

Figure 8. Dip latitudinal variation of zonally averaged NmF2 and hmF2 as a function of day number predicted by ANNIM at (top panels) varying and (bottom panels) constant Kp-index values of 2008. The superimposed black curve shows the daily averaged Kp-index and F10.7 solar flux during 2008.

based Digisonde network during the year 2008. The day time (8 to 16 LT) values of NmF2 and hmF2 in each day are binned into 2.5° dip latitude grids, and the data points in each bin, which corresponds to different longitudes, are averaged to compute the zonally (longitudinally) averaged NmF2 and hmF2 as shown in Figures 7a and 7b, respectively. The black curves with vertical axis on the right side represent the variation of the daily mean Kp index during the year 2008. It can be seen from Figures 7a and 7b that both the zonal mean NmF2 and hmF2 exhibit shorter time scale variations coherently with the Kp-index in addition to the longer time scale seasonal and semiannual variations. To further examine the short-scale variations, the daily variations of zonal mean NmF2 and hmF2 at each latitudinal bin have been subjected to the Lomb-Scargle (LS) periodogram (Lomb, 1976; Scargle, 1982) analysis as shown in Figures 7c and 7d. The white curves in Figures 7c and 7d with right-hand side vertical axis represent the LS periodogram of the daily mean Kp index during 2008. It can be seen from these figures that both NmF2 and hmF2 exhibit periodicities with strong spectral peaks at solar rotational (27-day) and its subharmonic (13.5 and 9-day) periodicities coherently with the similar variations of the Kp index. Tulasi Ram, Liu, et al. (2010) have clearly shown that the short period (13.5 and 9-day) oscillations in the ionosphere are mainly due to the recurrent CIR driven geomagnetic activity while the 27-day periodicity can be partly due to the variations in solar EUV irradiance.

In the present work, we have performed two controlled simulations using the ANNIM in order to examine whether the ANNIM can reproduce these coherent NmF2 and hmF2 variations in response to the recurrent geomagnetic activity. In the first simulation, the actual daily mean Kp-index and F10.7 solar flux values during the year 2008 are fed to the model and the NmF2 and hmF2 values at a fixed local time of 12 LT are derived from ANNIM at every 10° longitude and 5° dip latitude intervals for the day numbers 1 to 366 in 2008. Then the zonally (longitudinally) averaged NmF2 and hmF2 are computed for each dip latitude bin for each day. Figures 8a and 8b (top panels) show the dip latitude variations of zonal mean NmF2 and hmF2 as a function of day number in 2008, respectively. The black curves with vertical axis on the right side represent the daily mean Kp in 2008. It can be seen from these Figures 8a and 8b that both NmF2 and hmF2 exhibit shorter scale recurrent oscillations (vertical band like structures) at all latitudes coherently with the Kp index in addition to the longer scale seasonal and semiannual variations. In the second simulation, the daily mean Kp-index was kept at a constant value of two (Kp = 2), and the F10.7 solar flux values are varied as per the actual values in 2008. All the other parameters are set similar to the first simulation. For example, Figures 8c and 8d (bottom panels) show the variations of zonal mean NmF2 and hmF2 as a function of dip latitude and day number with

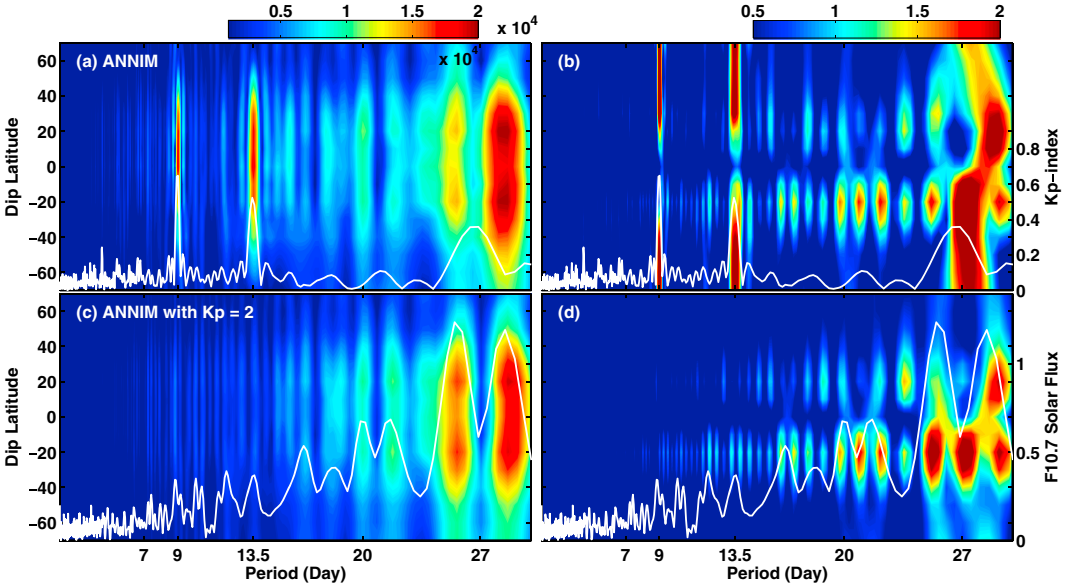

Figure 9. Lomb-Scargle periodogram of (left panels) NmF2 and (right panels) hmF2 values predicted by ANNIM in Figure 8 under (top panels) varying and (bottom panels) constant Kp-index values. The super imposed white curves represent the periodogram of daily averaged (top panels) Kp-index and (in bottom panels) F10.7 solar flux values of 2008, respectively.

the Kp fixed at 2. The black curves in Figures 8c and 8d with right-hand side axis indicate the daily F10.7 solar flux variations. It can be seen from these figures (Figures 8c and 8d) that the shorter scale oscillations (vertical band line structures) in NmF2 and hmF2 due to recurrent geomagnetic activity are distinctly absent when the Kp-index is set to a constant value of 2. However, clear variations in NmF2 and hmF2 in response to enhancements in F10.7 solar flux (e.g., around day numbers 88 and 291) can be clearly seen in addition to the longer scale seasonal and semiannual variations.

In order to further examine the periodicities in NmF2 and hmF2 variations during both the simulations, LS periodograms have been computed. Figure 9 shows the LS-periodograms of the ANNIM results obtained from simulation-1 (top panels) and simulation-2 (bottom panel). Figures 9a and 9b show the LS periodograms of NmF2 and hmF2 variations, respectively, predicted by ANNIM under varying Kp-index (simulation-1). Similarly, Figures 9c and 9d show the LS periodograms of NmF2 and hmF2 variations under a constant Kp-index (Kp = 2, simulation-2). The super imposed white curves in the top and bottom panels of Figure 9 represent the LS periodograms of daily averaged Kp-index and daily F10.7 solar flux during 2008, respectively. While the 27-day periodicity can be seen in both F10.7 solar flux and Kp-index, one can also observe the pronounced and sharp spectral peaks at 9- and 13.5-day periods only in the Kp-index due to the recurrent geomagnetic activity associated with HSS-CIR structures during 2008 (Tulasi Ram, Lei, et al., 2010 and Tulasi Ram, Liu, et al., 2010). From Figures 9a and 9b, it can be noted that along with the 27-day periodicity, the ANNIM-predicted NmF2 and hmF2 values exhibited sharp spectral peaks at 9- and 13.5-day periods that are well correlated with the corresponding periodicities in the Kp-index. The spectral peaks at 9- and 13.5-day are clearly absent in both NmF2 and hmF2 during the simulation-2 with a constant Kp-index set at 2 (Figures 9c and 9d) and LS periodogram resembles more or less similar to that of F10.7 spectrum. Therefore, from the results presented in Figures 8 and 9, one can conclude that the ANNIM has successfully reproduced the NmF2 and hmF2 responses to recurrent CIR-driven geomagnetic activity during the deep solar minimum 2008 and the model has the potential to perform controlled simulations to distinguish the roles of geomagnetic activity (Kp) and solar irradiance (F10.7 solar flux).

4. Summary and Conclusions

This paper presents an improved version of the two-dimensional ANNIM developed using long-term NmF2 and hmF2 data from RO observations of FORMOSAT-3/COSMIC, CHAMP, and GRACE, and nearly two decades of data from the GIRO Digisonde network. The global NmF2 and hmF2 data are binned into 840 spatial grids

of 5° dip latitude and 15° geographic longitude bins and the data in each spatial grid are trained using feed-forward neural network with error back propagation algorithm. The improved ANNIM has well captured the temporal (local time, seasonal, and solar cycle epoch) and spatial (latitude and longitude) variations of F2-layer peak density (NmF2) and altitude (hmF2). One of the significant improvements in this version of ANNIM (with respect to that of ST2017) is the successful reproduction of postsunset enhancements in equatorial hmF2 due to PRE (Figures 5d and 5f). While comparing with the ground-based Digisonde observations at Jicamarca, the ANNIM predictions of NmF2 and hmF2 are found to be as good as the IRI-2016 model (Figures 3 and 4). Further, the ANNIM has successfully captured the global scale F2 layer anomalies such as ionospheric annual anomaly, EIA, and its hemispheric asymmetries during solstices (Figures 5a and 5c).

The ANNIM simulations under disturbed geomagnetic conditions (Kp = 6) predict the depletion in NmF2 at auroral latitudes and an enhancement in low latitude to midlatitude in comparison with quiet geomagnetic conditions (Kp = 2; Figure 5c), which are consistent with the storm time meridional wind circulation and the associated neutral composition (O/N2 density ratio) changes reported in the earlier studies. The ANNIM predicts an enhancement in the F2-layer peak altitudes around auroral latitudes (Figure 5f) during disturbed geomagnetic activity, which is consistent with the increased plasma scale height at auroral latitudes due to particle precipitation and Joule heating at auroral latitudes. The controlled simulation of ANNIM with varying Kp has successfully reproduced the recurrent oscillations in NmF2 and hmF2 coherently with the recurrent geomagnetic activity associated with the recurrent HSS-CIR structures during the deep solar minimum 2008 (Figures 8 and 9). While the second controlled simulation of ANNIM with Kp fixed at 2 exhibits only the 27-day periodicity associated with varying F10.7 solar flux, but the short period oscillations at 13.5 and 9-day periods are absent. This indicates the potential of ANNIM to perform controlled simulations to distinguish the NmF2 and hmF2 variations associated with the recurrent geomagnetic activity (Kp) and the varying solar irradiance (F10.7 solar flux).

Ionospheric electron density is nonstationary and continuously varies due to the changes in production, loss and transport processes. The physics-based models that solve the conservation (continuity, momentum, and energy) equations can predict the continuously varying electron density for several hours/days once the necessary input conditions are initialized. However, the ANNIM is essentially an empirical model primarily driven by the long-term GPS-RO data and ground-based GIRO observations. Hence, the ANNIM can only predict the ionospheric F2-layer peak altitude (hmF2) and density (NmF2) for the given instance of input conditions similar to the other empirical models. With this successful development of two-dimensional ANNIM, we are currently working on the development of complete three-dimensional model by assimilating the vertical electron density profile data from GPS-RO missions, ground-based Digisondes and, if available, topside sounders. This would also enable us to predict the vertical total electron content, which is an important ionospheric parameter for satellite-based communication and navigational applications.

Acknowledgments
The F3/C, CHAMP, and GRACE RO data are obtained from UCAR-CDAAC (http://cdaac-www.cosmic.ucar.edu/cdaac/products.html). We sincerely acknowledge the contributors of GIRO-DIDBase team for providing the global Digisonde data through GIRO-DIDBase (http://giro.uml.edu/didbase/scaled.php).

References

Altinay, O., Tulunay, E., & Tulunay, Y. (1997). Forecasting of ionospheric critical frequency using neural networks. *Geophysical Research Letters*, *24*(12), 1467–1470. https://doi.org/10.1029/97GL01381

Anderson, D. N., Buonsanto, M. J., Codrescu, M., Decker, D., Fesen, C. G., Fuller-Rowell, T. J., et al. (1998). Intercomparison of physics models and observations of the ionosphere. *Journal of Geophysical Research*, *103*(A2), 2179–2192. https://doi.org/10.1029/97JA02872

Appleton, E. V. (1946). Two anomalies in the ionosphere. *Nature*, *157*(3995), 691. Bibcode:1946Natur.157.691A. https://doi.org/10.1038/157691a0

Bailey, G. J., & Balan, N. (1996). A low-latitude ionosphere-plasmasphere model. In R. W. Schunk (Ed.), *STEP Handbook on Ionospheric Models* (pp. 173–206). Logan: Utah State Univ.

Baker, D. N., Li, X., Pulkkinen, A., Ngwira, C. M., Mays, M. L., Galvin, A. B., & Simunac, K. D. C. (2013). A major solar eruptive event in July 2012: Defining extreme space weather scenarios. *Space Weather*, *11*, 585–591. https://doi.org/10.1002/swe.20097

Balan, N., Ebihara, Y., Skoug, R., Shiokawa, K., Batista, I. S., Tulasi Ram, S., et al. (2017). A scheme for forecasting severe space weather. *Journal of Geophysical Research: Space Physics*, *122*, 2824–2835. https://doi.org/10.1002/2016JA023853

Balan, N., Skoug, R., Tulasi Ram, S., Rajesh, P. K., Shiokawa, K., Otsuka, Y., et al. (2015). CME front and severe space weather. *Journal of Geophysical Research: Space Physics*, *119*, 10,041–10,058. https://doi.org/10.1002/2014JA020151

Bellchambers, W. H., & Piggott, W. R. (1958). Ionospheric measurements made at Halley Bay. *Nature*, *182*(4649), 1596–1597. https://doi.org/10.1038/1821596a0

Berkner, L. V., & Wells, H. W. (1938). Non-seasonal change of F2-region ion density. *Terrestrial Magnetism and Atmospheric Electricity*, *43*(1), 15–36. https://doi.org/10.1029/TE043i001p00015

Bilitza, D., Altadill, D., Truhlik, V., Shubin, V., Galkin, I., Reinisch, B., & Huang, X. (2017). International Reference Ionosphere 2016: From ionospheric climate to real-time weather predictions. *Space Weather*, *15*, 418–429. https://doi.org/10.1002/2016SW001593

Brahmanandam, P. S., Chu, Y. H., Wu, K. H., Hsia, H. P., Su, C. L., & Uma, G. (2011). Vertical and longitudinal electron density structures of equatorial E- and F-regions. *Annales de Geophysique*, *29*(1), 81–89. https://doi.org/10.5194/angeo-29-81-2011

Burns, A. G., Wang, W., Qian, L., Solomon, S. C., Zhang, Y., Paxton, L. J., & Yue, X. (2014). On the solar cycle variation of the winter anomaly. *Journal of Geophysical Research: Space Physics*, *119*, 4938–4949. https://doi.org/10.1002/2013JA019552

Bust, G. S., & Mitchell, C. N. (2008). History, current state, and future directions of ionospheric imaging. *Reviews of Geophysics*, *46*, RG1003. https://doi.org/10.1029/2006RG000212

Crowley, G., Reynolds, A., Thayer, J. P., Lei, J., Paxton, L. J., Christensen, A. B., et al. (2008). Periodic modulations in thermospheric composition by solar wind high speed streams. *Geophysical Research Letters*, *35*, L21106. https://doi.org/10.1029/2008GL035745

Drob, D. P., Emmert, J. T., Meriwether, J. W., Makela, J. J., Doornbos, E., Conde, M., et al. (2015). An update to the Horizontal Wind Model (HWM): The quiet time thermosphere. *Earth and Space Science*, *2*, 301–319. https://doi.org/10.1002/2014EA000089

Fuller-Rowell, T. J., Codrescu, M. V., Moffett, R. J., & Quegan, S. (1994). Response of the thermosphere and ionosphere to geomagnetic storms. *Journal of Geophysical Research*, *99*, 3893–3914.

Fuller-Rowell, T. J., Rees, D., Quegan, S., Moffett, R. J., Codrescu, M. V., & Millward, G. H. (1996). A coupled thermosphere-ionosphere model (CTIM). In R. W. Schunk (Ed.), *STEP: Handbook of ionospheric models* (pp. 217–238). Logan, Utah: Utah State University.

Galkin, I. A., Khmyrov, G. M., Kozlov, A. V., Reinisch, B. W., Huang, X., & Paznukhov, V. V. (2008). The ARTIST 5, in radio sounding and plasma physics. *AIP Conf. Proc.*, *974*, 150–159. https://doi.org/10.1063/1.2885024

Gaunt, C. T. and Coetzee, G. (2007). Transformer failures in regions incorrectly considered to have low GIC-risk, 2007 IEEE Lausanne Power Tech, Lausanne, pp. 807–812. https://doi.org/10.1109/PCT.2007.4538419

Habarulema, J. B., McKinnell, L.-A., & Opperman, B. D. L. (2011). Regional GPS TEC modeling; attempted spatial and temporal extrapolation of TEC using neural networks. *Journal of Geophysical Research*, *116*, A04314. https://doi.org/10.1029/2010JA016269

Huba, J. D., Joyce, G., & Fedder, J. A. (2000). Sami2 is another model of the ionosphere (SAMI2): A new low-latitude ionosphere model. *Journal of Geophysical Research*, *105*(A10), 23,035–23,053. https://doi.org/10.1029/2000JA000035

Huba, J. D., Joyce, G., & Krall, J. (2008). Three-dimensional equatorial spread F modeling. *Geophysical Research Letters*, *35*, L10102. https://doi.org/10.1029/2008GL033509

Krasnopolsky, V. M., & Lin, Y. (2012). A neural network nonlinear multimodel ensemble to improve precipitation forecasts over continental US. *Advances in Meteorology*, 649450, 1–11. https://doi.org/10.1155/2012/649450

Kumluca, A., Tulunay, E., Topalli, I., & Tulunay, Y. (1999). Temporal and spatial forecasting of ionospheric critical frequency using neural networks. *Radio Science*, *34*(6), 1497–1506. https://doi.org/10.1029/1999RS900070

Lamming, X., & Cander, L. R. (1999). Monthly median foF2 modelling COST 251 area by neural networks. *Physics and Chemistry of the Earth - Part C*, *24*, 349–354.

Leandro, R. F., & Santos, M. C. (2007). A neural network approach for regional vertical total electron content modelling. *Studia Geophysica et Geodaetica*, *51*(2), 279–292. https://doi.org/10.1007/s11200-007-0015-6

Lei, J., Syndergaard, S., & Burns, A. G. (2007). Comparison of COSMIC ionospheric measurements with ground-based observations and model predictions: Preliminary results. *Journal of Geophysical Research*, *112*, A07308. https://doi.org/10.1029/2006JA012240

Lei, J., Thayer, J. P., Forbes, J. M., Sutton, E. K., & Nerem, R. S. (2008). Rotating solar coronal holes and periodic modulation of the upper atmosphere. *Geophysical Research Letters*, *35*, L10109. https://doi.org/10.1029/2008GL033875

Lei, J., Thayer, J. P., Forbes, J. M., Sutton, E. K., Nerem, R. S., Temmer, M., & Veronig, A. M. (2008). Global thermospheric density variations cause by high-speed solar wind streams during the declining phase of solar cycle 23. *Journal of Geophysical Research*, *113*, A11303. https://doi.org/10.1029/2008JA013433

Levenberg, K. (1944). A method for the solution of certain non-linear problems in least squares. *Quarterly of Applied Mathematics*, *2*(2), 164–168. https://doi.org/10.1090/qam/10666

Lin, C. H., Liu, C. H., Liu, J. Y., Chen, C. H., Burns, A. G., & Wang, W. (2010). Mid-latitude summer nighttime anomaly of the ionospheric electron density observed by FORMOSAT-3/COSMIC. *Journal of Geophysical Research*, *115*, A03308. https://doi.org/10.1029/2009JA014084

Lin, C. H., Wang, W., Hagan, M. E., Hsiao, C. C., Immel, T. J., Hsu, M. L., et al. (2007). Plausible effect of atmospheric tides on the equatorial ionosphere observed by the FORMOSAT-3/COSMIC: Three-dimensional electron density structures. *Geophysical Research Letters*, *34*, L11112. https://doi.org/10.1029/2007GL029265

Liu, H., Thampi, S. V., & Yamamoto, M. (2010). Phase reversal of the diurnal cycle in the mid-latitude ionosphere. *Journal of Geophysical Research*, *115*, A01305. https://doi.org/10.1029/2009JA014689

Lomb, N. R. (1976). Least-squares frequency analysis of unequally spaced data. *Astrophysics and Space Science*, *39*(2), 447–462. https://doi.org/10.1007/BF00648343

Ma, X. F., Maruyama, T., Ma, G., & Takeda, T. (2005). Three-dimensional ionospheric tomography using observation data of GPS ground receivers and ionosonde by neural network. *Journal of Geophysical Research*, *110*, A05308. https://doi.org/10.1029/2004JA010797

MacAlester, M. H., & Murtagh, W. (2014). Extreme space weather impact: An emergency management perspective. *Space Weather*, *12*, 530–537. https://doi.org/10.1002/2014SW001095

Marquardt, D. W. (1963). An algorithm for the least-squares estimation of nonlinear parameters. *SIAM Journal of Applied Mathematics*, *11*(2), 431–441. https://doi.org/10.1137/0111030

Oyeyemi, E. O., & Poole, A. W. V. (2004). Towards the development of a new global foF2 empirical model using neural networks. *Advances in Space Research*, *34*(9), 1966–1972. https://doi.org/10.1016/j.asr.2004.06.010

Oyeyemi, E. O., Poole, A. W. V., & McKinnell, L. A. (2005). On the global model for foF2 using neural networks. *Radio Science*, *40*, RS6011. https://doi.org/10.1029/2004RS003223

Potula, B. S., Chu, Y.-H., Uma, G., Hsia, H.-P., & Wu, K.-H. (2011). A global comparative study on the ionospheric measurements between COSMIC radio occultation technique and IRI model. *Journal of Geophysical Research*, *116*, A02310. https://doi.org/10.1029/2010JA015814

Radicella, S. M., & Leitinger, R. (2001). The evolution of the DGR approach to model electron density profiles. *Advances in Space Research*, *27*(1), 35–40. https://doi.org/10.1016/S0273-1177(00)00138-1

Reinisch, B. W., & Galkin, I. A. (2011). Global Ionospheric Radio Observatory (GIRO). *Earth, Planets and Space*, *63*(4), 377–381. https://doi.org/10.5047/eps.2011.03.001

Reinisch, B. W., Galkin, I. A., Khmyrov, G. M., Kozlov, A. V., Bibl, K., Lisysyan, I. A., et al. (2009). The New Digisonde for Research and Monitoring Applications. *Radio Science*, *44*, RS0A24. https://doi.org/10.1029/2008RS004115

Richmond, A. D., Ridley, E. C., & Roble, R. G. (1992). A thermosphere/ionosphere general circulation model with coupled electrodynamics. *Geophysical Research Letters*, *6*, 601–604.

Rishbeth, H., & Setty, C. S. G. K. (1961). The F-layer at sunrise. *Journal of Atmospheric and Terrestrial Physics*, *21*, 263–276.

Rumelhart, D. E., Hinton, G. E., & Williams, R. (1986). Learning representations by back-propagating errors. *Nature*, *323*(6088), 533–536. https://doi.org/10.1038/323533a0

Sai Gowtam, V., & Tulasi Ram, S. (2017a). An artificial neural network based ionospheric model to predict NmF2 and hmF2 using long-term data set of FORMOSAT-3/COSMIC radio occultation observations: Preliminary results. *Journal of Geophysical Research: Space Physics*, *122*, 11,743–11,755. https://doi.org/10.1002/2017JA024795

Sai Gowtam, V., & Tulasi Ram, S. (2017b). Ionospheric annual anomaly—New insights to the physical mechanisms. *Journal of Geophysical Research: Space Physics*, *122*, 8816–8830. https://doi.org/10.1002/2017JA024170

Sai Gowtam, V., & Tulasi Ram, S. (2017c). Ionospheric winter anomaly and annual anomaly observed from Formosat-3/COSMIC radio occultation observations during the ascending phase of solar cycle 24. *Advances in Space Research*, *60*(8), 1585–1593. https://doi.org/10.1016/j.asr.2017.03.017

Scargle, J. D. (1982). Studies in astronomical time series analysis. II. Statistical aspects of spectral analysis of unevenly spaced data. *The Astrophysical Journal*, *263*, 835–853. https://doi.org/10.1086/160554

Schreiner, W. S., Rocken, C., Sokolovskiy, S., Syndergaard, S., & Hunt, D. C. (2007). Estimates of the precision of GPS radio occultation from the COSMIC/FORMOSAT-3 mission. *Geophysical Research Letters*, *34*, L04808. https://doi.org/10.1029/2006GL027557

Schunk, R. (2013). Ionospheric Models for Earth. In M. Mendillo, A. Nagy, & J. H. Waite (Eds.), *Atmospheres in the Solar System: Comparative Aeronomy* (chap. IV, Vol. 130, pp. 299–306). *American Geophysical Union*. https://doi.org/10.1029/130GM19

Sojka, J. J., McPherron, R. L., van Eyken, A. P., Nicolls, M. J., Heinselman, C. J., & Kelly, J. D. (2009). Observations of ionospheric heating during the passage of solar coronal hole fast streams. *Geophysical Research Letters*, *36*, L19105. https://doi.org/10.1029/2009GL039064

Strickland, D. J., Daniell, R. E., & Craven, J. D. (2001). Negative ionospheric storm coincident with DE 1-observed thermospheric disturbance on October 14, 1981. *Journal of Geophysical Research*, *106*, 21,049–21,062.

Thayer, J. P., Lei, J., Forbes, J. M., Sutton, E. K., & Nerem, R. S. (2008). Thermospheric density oscillations due to periodic solar wind high-speed streams. *Journal of Geophysical Research*, *113*, A06307. https://doi.org/10.1029/2008JA013190

Thébault, E., Finlay, C. C., Beggan, C. D., Alken, P., Aubert, J., Barrois, O., et al. (2015). International Geomagnetic Reference Field: The 12th generation. *Earth, Planets and Space*, *67*(1), 79. https://doi.org/10.1186/s40623-015-0228-9

Tulasi Ram, S., Lei, J., Su, S.-Y., Liu, C. H., Lin, C. H., & Chen, W. S. (2010). Dayside ionospheric response to recurrent geomagnetic activity during the extreme solar minimum of 2008. *Geophysical Research Letters*, *37*, L02101. https://doi.org/10.1029/2009GL041038

Tulasi Ram, S., Liu, C. H., & Su, S.-Y. (2010). Periodic solar wind forcing due to recurrent coronal holes during 1996–2009 and its impact on Earth's geomagnetic and ionospheric properties during the extreme solar minimum. *Journal of Geophysical Research*, *115*, A12340. https://doi.org/10.1029/2010JA015800

Tulasi Ram, S., Sandeep, K., Su, S.-Y., Veenadhari, B., & Ravindran, S. (2015). The influence of Corotating interaction region (CIR) driven geomagneticstorms on the development of equatorial plasma bubbles (EPBs) over wide range of longitudes. *Advances in Space Research*, *55*(2), 535–544. https://doi.org/10.1016/j.asr.2014.10.013

Tulasi Ram, S., Su, S.-Y., & Liu, C. H. (2009). FORMOSAT-3/COSMIC observations of seasonal and longitudinal variations of equatorial ionization anomaly and its interhemispheric asymmetry during the solar minimum period. *Journal of Geophysical Research*, *114*, A06311. https://doi.org/10.1029/2008JA013880

Tulunay, E., Senalp, E. T., Radicella, S. M., & Tulunay, Y. (2006). Forecasting total electron content maps by neural network technique. *Radio Science*, *41*, RS4016. https://doi.org/10.1029/2005RS003285

Tulunay, Y. K., & Bradley, P. A. (2004). The impact of space weather on communication. *Annals of Geophysics*, *47*, 929–944.

Uma, G., Brahmanandam, P. S., & Chu, Y. H. (2016). A long-term study on the deletion criterion of questionable electron density profiles caused by ionospheric irregularities–COSMIC radio occultation technique. *Advances in Space Research*, *57*(12), 2452–2463. https://doi.org/10.1016/j.asr.2016.03.034

Wan, W., Liu, L., Pi, X., Zhang, M. L., Ning, B., Xiong, J., & Ding, F. (2008). Wavenumber-4 patterns of the total electron content over the low latitude ionosphere. *Geophysical Research Letters*, *35*, L12104. https://doi.org/10.1029/2008GL033755

Watthanasangmechai, K., Supnithi, P., Lerkvaranyu, S., Tsugawa, T., Nagatsuma, T., & Maruyama, T. (2012). TEC prediction with neural network for equatorial latitude station in Thailand. *Earth, Planet and Space*, *64*(6), 473–483. https://doi.org/10.5047/eps.2011.05.025

Williscroft, L.-A., & Poole, A. W. A. (1996). Neural networks, foF2, sunspot number and magnetic activity. *Geophysical Research Letters*, *23*(24), 3659–3662. https://doi.org/10.1029/96GL03472

Wintoft, P. (2000). Twenty-four hour predictions of foF2 using neural networks. *Radio Science*, *35*, 395–408.

Yang, K. F., Chu, Y. H., Su, C. L., Ko, H. T., & Wang, C. Y. (2009). An examination of FORMOSAT-3/COSMIC ionospheric electron density profile: Data quality criteria and comparisons with the IRI model. *Terrestrial, Atmospheric and Oceanic Sciences*, *20*(1), 193–206. https://doi.org/10.3319/TAO.2007.10.05.01(F3C)

Zhao, X., Ning, B., Liu, L., & Song, G. (2014). A prediction model of short-term ionospheric foF2 based on AdaBoost. *Advances in Space Research*, *53*(3), 387–394. https://doi.org/10.1016/j.asr.2013.12.001

Zhou, C., Wang, R., Lou, W., Liu, J., Ni, B., Deng, Z., & Zhao, Z. (2013). Preliminary investigation of real-time mapping of foF2 in northern China based on oblique ionosonde data. *Journal of Geophysical Research: Space Physics*, *118*, 2536–2544. https://doi.org/10.1002/jgra.50262